ACS APPLIED MATERIALS & INTERFACES
Research Article
www.acsami.org

Semiconductor Behavior of a Three-Dimensional Strontium-Based Metal–Organic Framework

Muhammad Usman,[†,‡,§] Shruti Mendiratta,[†] Sainbileg Batjargal,[‡,§,∥] Golam Haider,[⊥,∇,#] Michitoshi Hayashi,[∥] Narsinga Rao Gade,[∥] Jenq-Wei Chen,[#] Yang-Fang Chen,[#] and Kuang-Lieh Lu*,[†]

[†]Institute of Chemistry, Academia Sinica, Taipei 115, Taiwan

[‡]Department of Physics, National Central University, Chung-Li 320, Taiwan

[§]Molecular Science and Technology, Taiwan International Graduate Program, Institute of Atomic and Molecular Science, Academia Sinica, Taipei 106, Taiwan

[∥]Center for Condensed Matter Sciences, National Taiwan University, Taipei 106, Taiwan

[⊥]Nano Science and Technology, Taiwan International Graduate Program, Academia Sinica, Taipei 106, Taiwan

[∇]National Tsing Hua University, Hsinchu 300, Taiwan

[#]Department of Physics, National Taiwan University, Taipei 106, Taiwan

Supporting Information

ABSTRACT: The self-assembly of a three-dimensional strontium-based metal–organic framework $[Sr(Hbtc)(H_2O)]_n$ (**1**) was achieved through the reaction of $Sr(NO_3)_2$ with a 1,2,4-benzenetricarboxylic acid (1,2,4-H_3btc) ligand under hydrothermal conditions. This Sr-based metal–organic framework exhibits remarkable semiconducting behavior, as evidenced by theoretical calculations and experimental measurements. Temperature-dependent DC conductivity, near-room-temperature AC conductivity, diffuse reflection spectra, and photoluminescence spectra provide strong proof that compound **1** shows a band gap of 2.3 eV, which is comparable to that for other commonly available semiconducting materials (e.g., CdSe, CdTe, ZnTe, GaP, etc.). The optimized molecular structure and electronic properties (density of states and band gap energy) of **1** were calculated using density functional theory, and the results are consistent with experimental findings. This is the first report on the semiconducting properties of a strontium-based MOF, which will pave the way for further studies in semiconducting MOFs with interesting potential applications in optoelectronic devices.

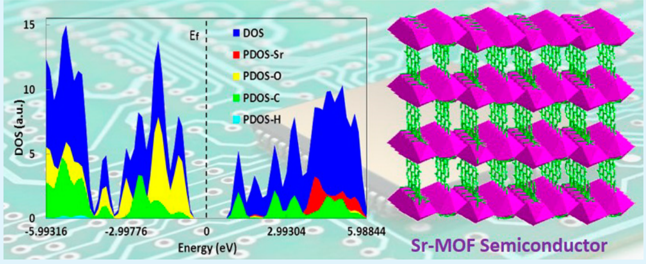

KEYWORDS: *bandgap, density functional theory, metal–organic framework, semiconductor, strontium*

1. INTRODUCTION

Expanding the dimensions of metal–organic framework (MOF) applications toward the electronics industry has been gaining momentum in recent years.[1−7] Because of their uniform porous structure and tunable functionalities,[8−17] MOFs have many potential applications in areas such as gas storage, sensing, chemical separations, catalysis, magnetic and optoelectronics, etc.[8−14,18−22] Allendorf and co-workers provided the roadmap for the implementation of MOFs in microelectronic devices.[23] However, understanding of the semiconducting behavior of MOFs is still in its initial stages and further investigations would be highly desirable.[24−31]

In 2007, Garcia and co-workers reported on the semiconductor behavior of MOF-5, which has a bandgap of 3.4 eV.[24] Since then, only a few reports on semiconducting properties of MOFs have appeared, in which Zn and Mg are mainly used as the metal nodes.[25−28] Considering the importance of strontium and its composites as effective semiconducting materials,[32−34] we envisaged that research directed toward strontium–organic frameworks would provoke great interest, because different organic ligands could be used, thus resulting in diverse structures with enhanced properties. Herein, we report on our investigations on the bandgap and semiconducting properties of a new type of Sr-based metal–organic framework $[Sr(Hbtc)(H_2O)]_n$ (**1**). Importantly, its band gap of 2.3 eV is comparable to that of other commonly used semiconducting materials (e.g., CdSe, CdTe, ZnTe, GaP, etc.).[35−37] To the best of our knowledge, this is the first example of a Sr-based MOF as a potential semiconductor in optoelectronic devices. The direction of this work may provide an effective path toward remarkable new applications of semiconducting MOFs in the future.

Received: December 29, 2014
Accepted: September 28, 2015
Published: September 28, 2015

DOI: 10.1021/acsami.5b07228
ACS Appl. Mater. Interfaces 2015, 7, 22767−22774

2. EXPERIMENTAL SECTION

2.1. Materials and Instruments. Chemical reagents were purchased commercially and were used as received without further purification. Diffraction measurements for compound **1** were carried out using a Bruker-Nonius Kappa CCD diffractometer with graphite-monochromated Mo Kα radiation (λ = 0.7107 Å). Data collection parameters of compound **1** are listed in Table S1 in the Supporting Information. Structure was solved using direct methods and refined using the SHELXL-97 program by full-matrix least-squares on F^2 values. All non-hydrogen atoms were refined anisotropically, while the hydrogen atoms were placed in ideal, calculated positions, with isotropic thermal parameters riding on their respective carbon atoms. Infrared spectra were recorded in the solid state (KBr pellets) on a Perkin−Elmer Model Paragon 1000 FT-IR spectrometer in the 4000−400 cm^{-1} range. Elemental analyses were conducted on a Perkin−Elmer Model 2400 CHN elemental analyzer. Thermogravimetric (TG) analyses were performed under nitrogen with a Perkin−Elmer Model TGA-7 TG analyzer. Differential scanning calorimetry (DSC) was performed using a Jupiter Model STA 449 F3 instrument. Experimental powder X-ray diffraction data were recorded on a Siemens D-5000 diffractometer at 40 kV, 30 mA for Cu Kα (λ = 1.5406 Å), with a step size of 0.004° and scan speed of 0.15 s per step. The simulated powder diffraction data was obtained from the crystal structure of **1**, using the "Mercury 1.4.1" software program. The AC conductivity, capacitance (C), and dielectric loss tangent (tan δ) measurements were carried out in the frequency range from 20 Hz to 1 MHz at temperatures between 16 K and 300 K, using an Agilent Model HP-4284A LCR meter and a Lakeshore temperature controller with a computer-controlled program. The measurements were performed over the temperature range from room temperature to 370 K, using an in-house-fabricated cooling−heating system under a vacuum (0.1 Pa or 1×10^{-3} Torr). For each measurement, the temperature was maintained constant within an accuracy of ±0.05 K. The single crystals were ground and pressed into pellets 0.4 cm in diameter, with thicknesses of 0.04−0.07 cm. The measurements were performed on these circular dish-shaped samples with silver paint coated on both sides as electrodes. We repeated experiments on samples with different thicknesses. The observed results are consistent within experimental errors. The possibility of extrinsic factors, such as trapped interfacial charge carriers and electrode effects, is minimal in our samples.

The real (ε') and imaginary (ε'') parts of the complex dielectric constant, and the AC conductivity (σ_{AC}), were calculated from raw data and the pertinent sample dimensions are as follows:

$$\varepsilon' = \frac{Ct}{\varepsilon_0 A}$$

$$\varepsilon'' = \varepsilon' \tan \delta$$

$$\sigma_{AC} = \omega C \tan \delta \left(\frac{t}{A} \right)$$

where C is the capacitance (F), t the sample thickness (cm), A the cross-sectional area (cm^2), and ε_0 the permittivity of free space ($\varepsilon_0 = 8.854 \times 10^{-14}$ F/cm). The photoluminescence (PL) spectrum of a pellet sample of compound **1** was taken under the illumination of pulsed 266 nm laser with a frequency of 10 Hz. The power of the laser varied from 25 μW to 55 μW. PL spectrum was collected by iHR 550 spectrometer coupled with Synapse CCD of Horiba Jobin Yvon. The diffuse reflection spectrum (DRS) was obtained on a Perkin−Elmer Model Lambda 750 UV−vis spectrometer. To measure the DRS, the power MOF was spin-coated on a SiO_2 substrate. Temperature-dependent DC conductivity has been obtained for compound **1** using current−voltage (I−V) measurements in the temperature range of 150−300 K, using the two-probe method. Silver tape was used to mount the sample onto the substrate.

2.2. Synthesis of $[Sr(Hbtc)(H_2O)]_n$ (1). A mixture of $Sr(NO_3)_2$ (21.2 mg, 0.1 mmol), 1,2,4-benzenetricarboxylic acid (21.0 mg, 0.1 mmol), acetone (3 mL), and H_2O (4 mL) was sealed in a Teflon-lined stainless steel Parr acid digestion bomb and heated at 120 °C for 72 h and then allowed to slowly cool to room temperature at a rate of 6 h/°C. Rectangular crystals of compound **1** were produced in 31.9% yield (20 mg, based on Sr(II)). The solid product was separated by filtration and washed with water, and dried at ambient temperature. Elemental analysis Calcd (%) for $C_9H_6O_7Sr$: C, 34.45; H, 1.93. Found (%): C, 34.16; H, 2.02. IR data (KBr, cm^{-1}): 3193(s), 3000(w), 2637(w), 2521(m), 2351(w), 1986(w), 1945(w), 1818(w), 1687(s), 1607(w), 1562(s), 1497(s), 1420(s), 1374(m), 1314(s), 1292(s), 1247(s), 1173(m), 1120(s), 980(w), 912(m), 855(s), 812(m), 765(s), 703(m), 668(m), 599(m), 568(s), 527(m).

2.3. Simulation Details. The Vienna Ab-initio Simulation Package (VASP)[38−41] was used to perform density functional theory (DFT) calculations to describe the electronic structure of compound **1**. The calculations were carried out with the generalized gradient approximations (GGA), as parametrized by Perdew, Burke, and Ernzerhof (PBE)[42,43] for exchange-correlation functions and projector augmented-wave (PAW)[44,45] potentials. Periodic models and a plane-wave cutoff of 520 eV were used in all of our calculations. The irreducible Brillouin zone was sampled with a Γ-centered Monkhorst−Pack 8 × 8 × 3 k-mesh.[46] The criterion to stop the relaxation of the electronic degrees of freedom was set by the total energy change to be smaller than 1×10^{-6} eV.

3. RESULTS AND DISCUSSION

3.1. Synthesis of $[Sr(Hbtc)(H_2O)]_n$ (1) and Structural Analysis. Self-assembly of a unique strontium compound $[Sr(Hbtc)(H_2O)]_n$ (**1**) was achieved by reacting equimolar amounts of $Sr(NO_3)_2$ and 1,2,4-benzenetricarboxylic acid (1,2,4-H_3btc) in an acetone/H_2O solution under hydrothermal conditions at 120 °C for a period of 3 days (see Scheme 1).

Scheme 1. Synthesis of Compound 1

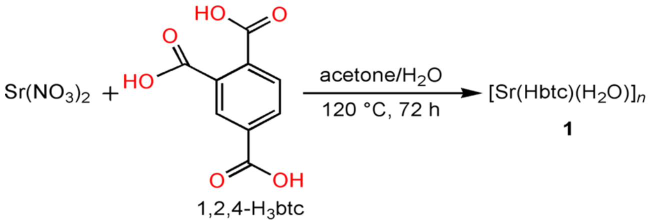

A single-crystal X-ray diffraction (XRD) analysis revealed that **1** adopts a three-dimensional (3D) framework and crystallizes in the triclinic $P\bar{1}$ space group (see Table S1 in the Supporting Information). The asymmetric unit of **1** consists of a single crystallographic site for strontium Sr(II), one $Hbtc^{2-}$ ligand and a coordinated water molecule, as illustrated in Figure 1a. The Sr center adopts a distorted square antiprism geometry, as determined by the donor atoms around the Sr(II) center, as illustrated in Figure S3 in the Supporting Information. The Sr center is eight-coordinated through seven oxygens (O1, O2, O2′, O3, O3′, O4, and O6) from five $Hbtc^{2-}$ ligands and one oxygen (O7) from a water molecule. The bond length of Sr−O falls in the range from 2.5049(65) Å to 2.7191(67) Å. The oxygen (O1, O2, O3, O4) atoms from the carboxylate groups (1, 2) of the ligand are coordinated to the Sr center in monodentate, chelating and bridged coordination modes, resulting in the formation of a two-dimensional (2D) layered structure (Figure 1c). The 2D layers of compound **1** are extended into a 3D network through a third carboxylate group of an $Hbtc^{2-}$ ligand. The pillar ligand functions as a bridge between two layers (Figure 1b). The H_2O molecules are stabilized around the layers by (O−H···O) hydrogen bonding interactions {(O5···O7 = 2.6075(104) Å); (O4···O7 =

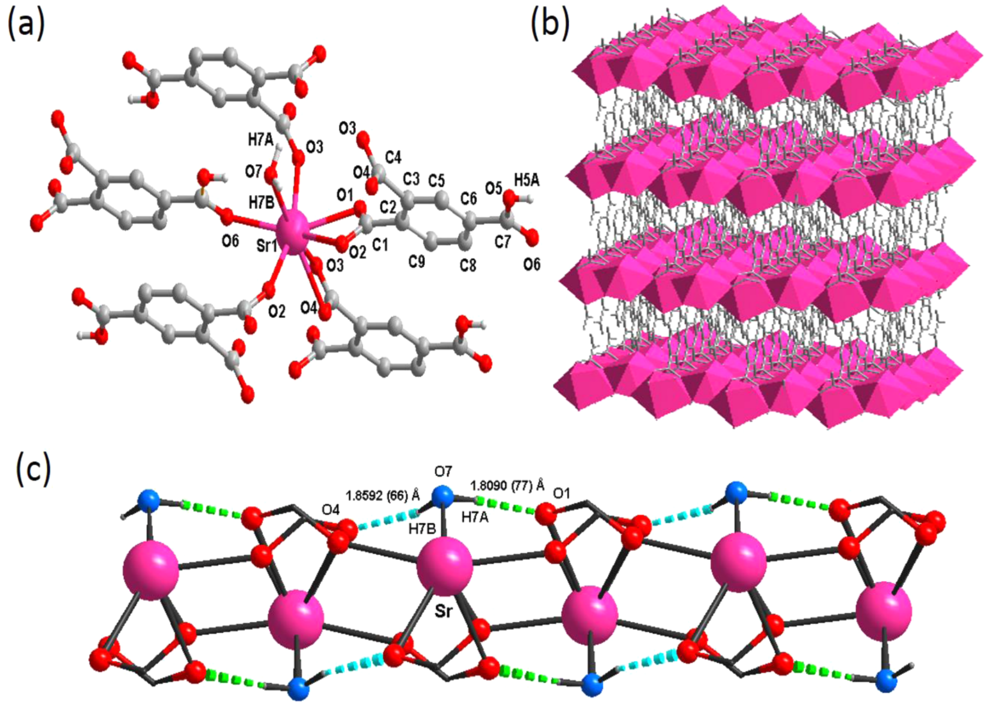

Figure 1. (a) Asymmetric unit of **1**. (b) A layered structure connected through pillar ligands. (c) Hydrogen bonding interactions of water molecules along the 2D layer of **1**.

2.6828(91) Å); (O1···O7 = 2.6574(113) Å)} (see Figure S4 in the Supporting Information). The crystal surface morphology can be visualized in the scanning electron microscopy (SEM) and optical microscopy images shown in Figure S5 in the Supporting Information.

3.2. Thermogravimetric Analysis and Powder X-ray Diffraction Studies.

A thermogravimetric analysis (TGA) of **1** indicates that the coordinated water molecules were lost in the temperature range of 65–270 °C (see Figure S6 in the Supporting Information). The observed weight loss of 5.5% is consistent with the calculated value (5.7%). After the loss of water molecules, the framework began to decompose with a continuous weight loss of 57.4% up to a temperature of 520 °C, which can be attributed to the loss of the coordinating ligand. The transition can also be observed during the heating of the compound, as shown in the differential scanning calorimetry (DSC) plot (see Figure S7 in the Supporting Information). The results of powder X-ray diffraction (PXRD) experiments showed that all of the peaks that were displayed in the measured patterns at room temperature closely matched those in the simulated patterns (see Figure S8 in the Supporting Information).

3.3. Electrical Characterization.

Temperature-dependent DC conductivity for compound **1** was obtained by I–V measurements in the temperature range of 150–300 K, using the two-probe method, as illustrated in the inset of Figure 2 and the DC electrical conductivity of **1** was found in the range of 10^{-6} (S cm^{-1}). Figure 2 shows that the conductivity of the MOF increases exponentially as the annealing temperature increases, and that the conductivity obeys Arrhenius plot (σ vs $1/T$), indicating that **1** has semiconducting transport behavior. The exponential increase in conductivity with temperature indicates that a major part of the conductivity is due to the contribution of thermally generated carriers and variable-range hopping, which is an indicator of the semiconducting nature of compound **1**.[47] The activation energy (E_a) was calculated from an Arrhenius plot for temperature-dependent DC conductivity and found to be 0.17 eV. The conductivity curve becomes almost stable at temperatures below 150 K, which could be due to low thermally generated carriers, which could then contribute to the conductivity at temperatures below 150 K. A room-temperature DC conductivity plot is shown in Figure S9 in the Supporting Information.

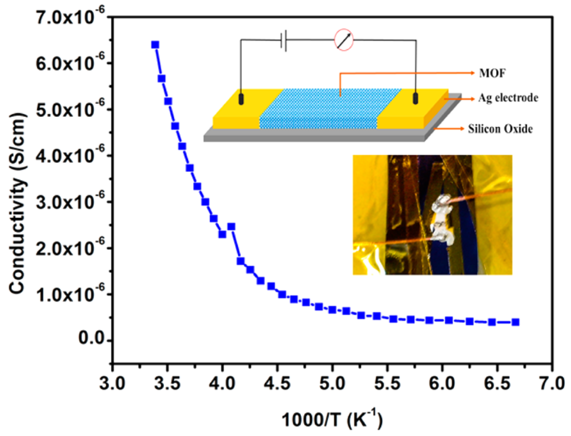

Figure 2. Arrhenius plot for the temperature-dependent DC conductivity for compound **1**. The device schematic and a photograph of the device are shown as insets.

The frequency-dependent conductivity $\sigma_{AC}(\omega)$ for compound **1** around room temperature is shown in Figure 3. It can be seen that the conductivity increases monotonically with frequency. A common feature of all amorphous semiconductors is that the AC conductivity $\sigma_{AC}(\omega)$ increases with frequency according to eq 1, where ω is the angular frequency, s the frequency exponent, and A a constant that is independent of frequency.[48]

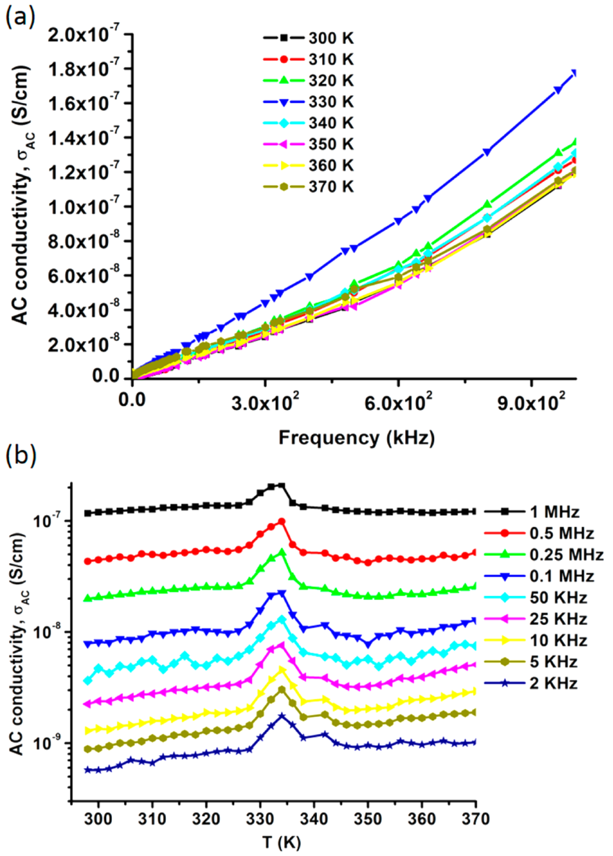

Figure 3. (a) AC conductivity versus frequency measurements for **1** at variable temperatures. (b) AC conductivity versus temperature at different frequencies.

$$\sigma_{\mathrm{AC}}(\omega) = \sigma_t(\omega) - \sigma_{\mathrm{DC}} = A\omega^s \tag{1}$$

An increase in conductivity can be observed with increasing frequency, which is a commonly observed phenomenon for polymeric and semiconductor materials.[49] The dominant mechanism responsible for the increase in $\sigma_{\mathrm{AC}}(\omega)$ with increasing frequency can be attributed to hopping conduction.[50] As shown in Figure 3, compound **1** shows an AC conductivity of 10^{-9}–10^{-7} S/cm, which is slightly increasing at variable temperatures. However, a small peak appears at 335 K for every applied frequency, which increases the conduction to a higher value, which then drops back with further increases in temperature. The observed peak is due to a dehydration process that involves the removal of water molecules.[27,51] As shown in Figure 1c, the coordinated water molecules are bonded in the layers of **1** through the coordination bonding and the weak hydrogen bonding interactions. When the temperature is increased to 335 K or higher, the water molecules begin to be released from the framework and, hence, a transition phase is observed at ~335 K (65 °C), as shown in the differential scanning calorimetry (DSC) data (see Figure S7 in the Supporting Information). They are completely evacuated at a temperature of ~540 K. However, the conductivity is almost constant as the temperature increases further to 370 K. This relatively weak temperature-dependent mechanism is also a confirmation of hopping between localized states around the Fermi level.[50]

The frequency dependence for the relative permittivity $[\varepsilon'_{\mathrm{r}}(\omega) + i\varepsilon''_{\mathrm{r}}(\omega)]$ of **1** was measured at variable temperatures, in which $\varepsilon'_{\mathrm{r}}(\omega)$ (dielectric constant) and $\varepsilon''_{\mathrm{r}}(\omega)$ (dielectric loss) are the respective real and imaginary parts of the permittivity. Figure 4 shows the variation in the dielectric constant $\varepsilon'_{\mathrm{r}}(\omega)$ and dielectric loss (tan δ) versus frequency as a function of temperature. The dielectric constant ($\varepsilon'_{\mathrm{r}}(\omega) \sim 13$) remains almost stable at high frequencies but a large decay is observed for compound **1** at low frequencies. The decrease in the dielectric constant $\varepsilon'_{\mathrm{r}}(\omega)$ and dielectric loss (tan δ) with frequency can be attributed to the inability of dipoles to rotate rapidly, thus leading to a lag between the frequency of the oscillating dipole and the applied field, which results in a loss of polarization.[27] The variation indicates that, at low frequencies, the dielectric constant is high, because of high interfacial, ionic, and electric polarizations. The dielectric loss (tan δ) is the energy dissipation in the dielectric system, which is proportional to the imaginary part of the dielectric constant ($\varepsilon''_{\mathrm{r}}(\omega)$). The dielectric loss (tan δ) becomes large at lower frequencies, reaching a value of 0.12 at 1 kHz, because of space charge polarization within the framework; however, at higher frequencies, these losses are reduced.[52,53] A dielectric relaxation peak can be observed for the relative permittivity (dielectric constant) and dielectric loss, which can be attributed to the removal of water molecules from the framework.[54] After compound **1** has been heated at 335 K, the coordinated water molecules begin to be released and interactions within the framework can dramatically change the activation enthalpy, thereby affecting the relaxation behavior and a peak is observed for the dielectric constant and dielectric loss at 335 K. Similar dielectric peaks are observed for geometric confinement of different liquids in nanopores.[55]

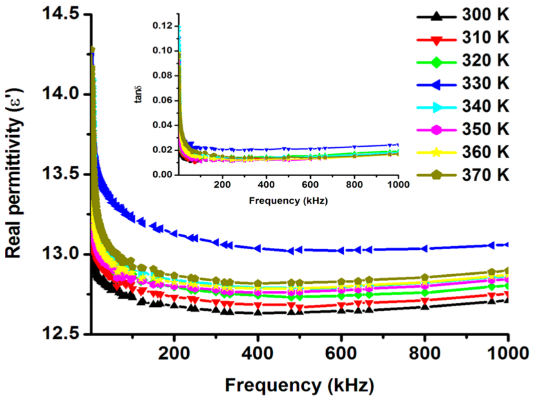

Figure 4. Frequency-dependent relative permittivity (ε') measurements at variable temperatures, the offset of the figure shows the dielectric loss (tan δ) for **1** at different temperatures.

3.4. Diffuse Reflection Spectrum.

To measure the reflection spectrum, the powder MOF was spin-coated on a SiO_2 substrate. The spectrum was obtained on a Perkin–Elmer Model Lambda 750 UV-vis spectrometer. An identical substrate was used to remove the effect of the substrate on the spectrum. Figure 5a shows the diffuse reflectance spectrum of a pelleted sample of compound **1**. A reflection peak can be observed at ~500–650 nm. The band gap was determined from the diffuse reflectance data using the Kubelka–Munk (KM) method, which is given by the following equation:

$$\frac{K}{S} = F(R) = \frac{(1 - R)^2}{2R}$$

where R is the reflectance, $F(R)$ is the KM function, and K and S are the absorption and scattering coefficients, respectively.

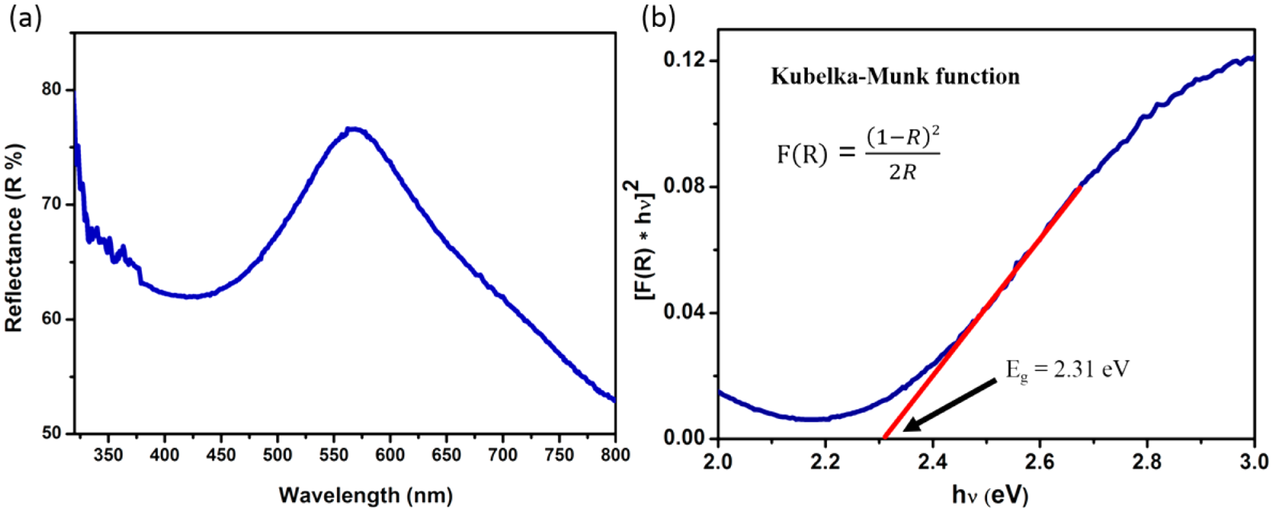

Figure 5. (a) Diffuse reflection spectrum for compound **1**; (b) Tauc plot ($[F(R) \times \hbar\upsilon]^2$ vs $\hbar\upsilon$) for bandgap transitions for **1**.

For allowed direct transitions, the optical band gap for compound **1** is determined by preparing a Tauc Plot ($[F(R) \times \hbar\upsilon]^2$ vs $\hbar\upsilon$) (Figure 5b). Extrapolation of this line to the photon energy axis yields a semiconductor band gap of 2.31 eV.[56,57]

3.5. Photoluminescence Study. A PL spectrum of **1** at a different power of excitation was obtained for direct bandgap observation. A very strong luminescence due to charge transfer is observed at room temperature under illumination from a 266 nm pulsed laser, as shown in Figure 6. The spectrum is composed of two separated peaks centered at ∼330 and 640 nm. The luminescence in the low-frequency region is further shown in the inset of Figure 6. The strong luminescence at ∼330 nm can be explained as a ligand-based emission, as shown in Figure S10 in the Supporting Information.[58] A relatively weak emission peak at 640 nm can be assigned to ligand-to-metal charge transfer (LMCT).[5,58] The peak at ∼640 nm indicates the existence of an optical band at ∼1.94 eV, which is further confirmed with theoretical calculations.

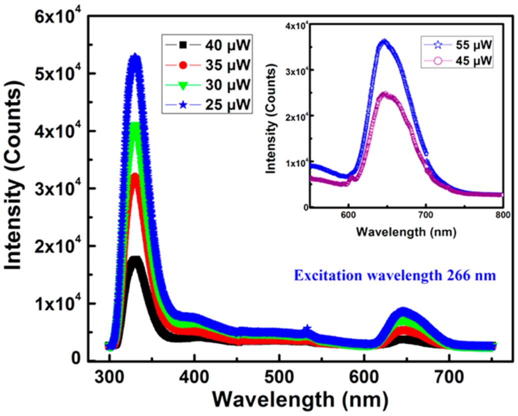

Figure 6. Photoluminescence (PL) spectra of **1** at a variable power of excitation. Inset shows a peak in the lower-frequency region.

3.6. Simulation Data. The electronic properties, such as the density of states and band-gap energy, were calculated using DFT. MOFs are a type of hybrid crystalline material that contains both organic and inorganic components. It is important to choose an appropriate simulation set that is suitable for describing electronic structure of the organic linkers, as well as for the metallic nodes. Starting with the experimentally determined unit cells of the framework of **1**, the atomic positions of [Sr(Hbtc)(H_2O)] were relaxed through minimizing the Hellmann−Feynman forces acting on each atom until the maximum forces on the ions were <0.001 eV/Å. The relaxed structure of the unit cell of **1** is shown in Figure S11 in the Supporting Information. The single crystal of $[\text{Sr(Hbtc)(H}_2\text{O)}]_n$ is a triclinic $P\bar{1}$ system with cell parameters of a = 6.85 Å, b = 7.01 Å, and c = 10.76 Å, and α = 87.65°, β = 82.61°, and γ = 72.06°.[38−47] We obtained the band structure, as well as the total and partial density of states (DOS and PDOS, respectively), of the $[\text{Sr(Hbtc)(H}_2\text{O)}]_n$, as shown in Figure 7.

The band structure along with high symmetry lines in the Brillouin zone are presented in Figure 7a. The dashed red line at 0 eV in Figure 7a indicates the Fermi level (E_F). The band-gap value was determined by the energy difference between the valence band maximum (VBM) and the conduction band minimum (CBM). The calculated value for the band-gap energy is 2.04 eV, which is in good agreement with the optical measurements of **1**. According to our calculations as in Figure 7a, the VBM is at the Γ-point, while the CBM is at the X-point in reciprocal space. The smallest band gap is indirect (Γ → X), between the Γ-point in the valence band and the X-point in the conduction band, being 2.04 eV. This confirms that the $[\text{Sr(Hbtc)(H}_2\text{O)}]_n$ crystal has semiconducting properties. In an analysis of the DOS depicted in Figure 7b, the blue area represents the total density of state (DOS), while the other areas represent the partial density of states (PDOS). It can be seen that the valence bands located below the Fermi level in the figure are composed of the states of the O, C, Sr, and H atoms (see Figure 7b, as well as Figures S12 and S13 in the Supporting Information). The conduction bands consist of the states of the C, O, and Sr atoms. The VBM mainly consists of the states of O atoms, as well as a small contribution from the states of the C and Sr atoms, while the CBM is dominantly composed of the states of the C and O atoms. None of the states of the H atoms are involved in the VBM or CBM around the E_F level. The band-gap energy of **1** is comparably lower than the reported values for MOF-5 (E_g = 3.4 eV)[24] and ZIF-8 (E_g = 5.5 eV)[59] but is very close to that of the IRMOFs[60] and some well-known semiconductor materials (such as CdSe, CdTe, ZnTe, GaP, etc.).[35−37]

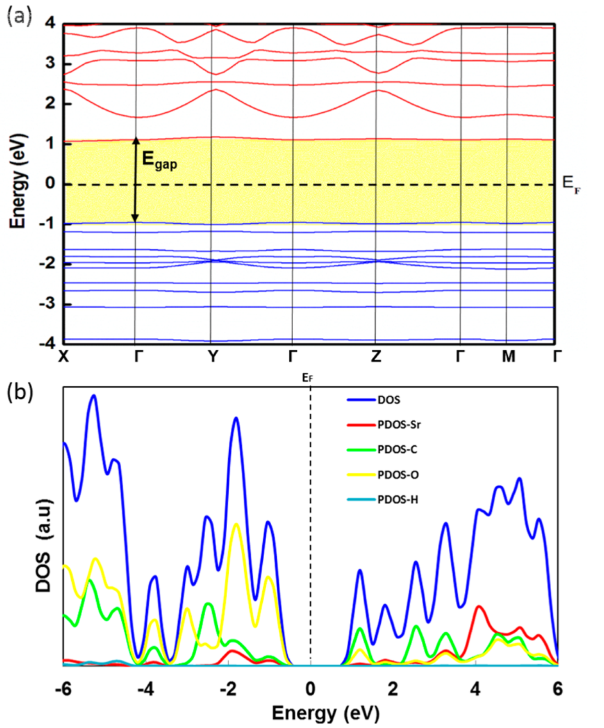

Figure 7. (a) Energy band gap structure of **1** (the dashed red line indicates the Fermi level (E_F)). (b) Total density of states (DOS) (blue line) and partial density of states (PDOS) (other colored area); the dashed line at zero energy represents the Fermi level (E_F).

4. CONCLUSION

In conclusion, a three-dimensional (3D) Sr-based metal–organic framework $[Sr(Hbtc)(H_2O)]_n$ (**1**) showed semiconductor behavior, as established by both experimental measurements and theoretical calculations. Significantly, compound **1** exhibited a band gap of 2.3 eV, which is comparable with other commonly used semiconducting materials (e.g., CdSe, CdTe, ZnTe, GaP, etc.). This work represents a significant and encouraging step toward a new research direction for potential applications of MOFs. In addition, these results provide strong justification for further studies of Sr-based MOFs, which may lead to the development of even more interesting semiconducting MOFs in the future.

■ ASSOCIATED CONTENT

Ⓢ Supporting Information

Crystal structure data for **1**: $C_{18}H_{12}O_{14}Sr_2$, $[Sr(Hbtc)(H_2O)]_n$, $M_r = 627.52$, Triclinic, $P\bar{1}$, $a = 6.8546$ (6) Å, $b = 7.0142$ (6) Å, $c = 10.7620$ (8) Å, α (deg) = 87.650 (5), β (deg) = 82.614 (5), γ (deg) = 72.056 (5), V = 488.18 (7) Å^3, Z = 1, $\rho_{calcd} = 2.134$ g/cm^3, $\mu = 5.955$ mm^{-1}, λ (Mo Kα) = 5.545 Å, F (000) = 308, T = 200 (2) K. Final R indices: $R_1 = 0.0689$, $wR_2 = 0.1818$ [$I > 2\sigma(I)$]; $R_1 = 0.0713$, $wR_2 = 0.1829$ [all data], GOF = 1.094. CCDC = 1011044 contains the supplementary crystallographic data for this paper. These data can be obtained free of charge from the Cambridge Crystallographic Data Centre via www.ccdc.cam.ac.uk/data_request/cif. The Supporting Information is available free of charge on the ACS Publications website at DOI: 10.1021/acsami.5b07228.

Crystal and structure refinement data (Table S1); IR spectra of ligands and compound **1** (Figure S1); coordination geometry for Sr (Figures S2 and S3); hydrogen bonding networks of **1** (Figure S4); surface morphology of single crystal (Figure S5); thermogravimetric analysis (TGA) of **1** (Figure S6); differential scanning calorimetry (DSC) plots (Figure S7); simulated and experimental powder X-ray patterns (Figure S8); room-temperature *I*–*V* characterization (Figure S9); photoluminescence spectrum of the organic ligand (Figure S10); optimized structure of **1** (Figure S11); indirect gap between Γ–X of the band structure (Figure S12); total and partial density of states (Figure S13) (PDF)

Crystallographic data for $C_{18}H_{12}O_{14}Sr_2$ (CIF)

■ AUTHOR INFORMATION

Corresponding Author

*Fax: +886-2-27831237. E-mail: kllu@gate.sinica.edu.tw.

Notes

The authors declare no competing financial interest.

■ ACKNOWLEDGMENTS

We gratefully acknowledge Academia Sinica, Taiwan for their financial support for the Ph.D. program through a platform of Taiwan International Graduate Program (TIGP). We also thank to the Ministry of Science and Technology, Taiwan, for their financial support.

■ REFERENCES

(1) Talin, A. A.; Centrone, A.; Ford, A. C.; Foster, M. E.; Stavila, V.; Haney, P.; Kinney, R. A.; Szalai, V.; El Gabaly, F.; Yoon, H. P.; Leonard, F.; Allendorf, M. D. Tunable Electrical Conductivity in Metal–Organic Framework Thin-Film Devices. *Science* **2014**, *343*, 66–69.

(2) Ramaswamy, P.; Wong, N. E.; Shimizu, G. K. MOFs as Proton Conductors–Challenges and Opportunities. *Chem. Soc. Rev.* **2014**, *43*, 5913–5932.

(3) Sheberla, D.; Sun, L.; Blood-Forsythe, M. A.; Er, S.; Wade, C. R.; Brozek, C. K.; Aspuru-Guzik, A.; Dinca, M. High Electrical Conductivity in Ni_3(2,3,6,7,10,11-Hexaiminotriphenylene)$_2$, a Semiconducting Metal-Organic Graphene Analogue. *J. Am. Chem. Soc.* **2014**, *136*, 8859–8862.

(4) Shen, L.; Yang, S. W.; Xiang, S.; Liu, T.; Zhao, B.; Ng, M. F.; Goettlicher, J.; Yi, J.; Li, S.; Wang, L.; Ding, J.; Chen, B.; Wei, S. H.; Feng, Y. P. Origin of Long-Range Ferromagnetic Ordering in Metal–Organic Frameworks with Antiferromagnetic Dimeric-Cu(II) Building Units. *J. Am. Chem. Soc.* **2012**, *134*, 17286–17290.

(5) Cui, Y.; Yue, Y.; Qian, G.; Chen, B. Luminescent Functional Metal–Organic Frameworks. *Chem. Rev.* **2012**, *112*, 1126–1162.

(6) Pan, C.; Nan, J.; Dong, X.; Ren, X. M.; Jin, W. A Highly Thermally Stable Ferroelectric Metal–Organic Framework and its Thin Film with Substrate Surface Nature Dependent Morphology. *J. Am. Chem. Soc.* **2011**, *133*, 12330–12333.

(7) Milios, C. J.; Vinslava, A.; Wernsdorfer, W.; Moggach, S.; Parsons, S.; Perlepes, S. P.; Christou, G.; Brechin, E. K. A Record Anisotropy Barrier for a Single-Molecule Magnet. *J. Am. Chem. Soc.* **2007**, *129*, 2754–2755.

(8) Zhou, H. C.; Long, J. R.; Yaghi, O. M. Introduction to Metal–Organic Frameworks. *Chem. Rev.* **2012**, *112*, 673–674.

(9) Furukawa, H.; Cordova, K. E.; O'Keeffe, M.; Yaghi, O. M. The Chemistry and Applications of Metal–Organic Frameworks. *Science* **2013**, *341*, 1230444.

(10) Nugent, P.; Belmabkhout, Y.; Burd, S. D.; Cairns, A. J.; Luebke, R.; Forrest, K.; Pham, T.; Ma, S.; Space, B.; Wojtas, L.; Eddaoudi, M.; Zaworotko, M. J. Porous Materials with Optimal Adsorption Thermodynamics and Kinetics for CO_2 Separation. *Nature* **2013**, *495*, 80–84.

(11) Yang, W.; Davies, A. J.; Lin, X.; Suyetin, M.; Matsuda, R.; Blake, A. J.; Wilson, C.; Lewis, W.; Parker, J. E.; Tang, C. C.; George, M. W.; Hubberstey, P.; Kitagawa, S.; Sakamoto, H.; Bichoutskaia, E.; Champness, N. R.; Yang, S.; Schröder, M. Selective CO_2 Uptake and Inverse CO_2/C_2H_2 Selectivity in a Dynamic Bifunctional Metal−Organic Framework. *Chem. Sci.* **2012**, *3*, 2993−2999.

(12) Kreno, L. E.; Leong, K.; Farha, O. K.; Allendorf, M.; Van Duyne, R. P.; Hupp, J. T. Metal−Organic Framework Materials as Chemical Sensors. *Chem. Rev.* **2012**, *112*, 1105−1125.

(13) Sakata, Y.; Furukawa, S.; Kondo, M.; Hirai, K.; Horike, N.; Takashima, Y.; Uehara, H.; Louvain, N.; Meilikhov, M.; Tsuruoka, T.; Isoda, S.; Kosaka, W.; Sakata, O.; Kitagawa, S. Shape-Memory Nanopores Induced in Coordination Frameworks by Crystal Downsizing. *Science* **2013**, *339*, 193−196.

(14) Salles, F.; Maurin, G.; Serre, C.; Llewellyn, P. L.; Knöfel, C.; Choi, H. J.; Filinchuk, Y.; Oliviero, L.; Vimont, A.; Long, J. R.; Férey, G. Multistep N_2 Breathing in the Metal−Organic Framework Co(1,4-benzenedipyrazolate). *J. Am. Chem. Soc.* **2010**, *132*, 13782−13788.

(15) Zhang, J. P.; Zhang, Y. B.; Lin, J. B.; Chen, X. M. Metal Azolate Frameworks: From Crystal Engineering to Functional Materials. *Chem. Rev.* **2012**, *112*, 1001−1033.

(16) Tian, D.; Chen, Q.; Li, Y.; Zhang, Y. H.; Chang, Z.; Bu, X.-H. A Mixed Molecular Building Block Strategy for the Design of Nested Polyhedron Metal−Organic Frameworks. *Angew. Chem., Int. Ed.* **2014**, *53*, 837−841.

(17) Luo, T. T.; Wu, H. C.; Jao, Y. C.; Huang, S. M.; Tseng, T. W.; Wen, Y. S.; Lee, G. H.; Peng, S. M.; Lu, K. L. Self-Assembled Arrays of Single-Walled Metal−Organic Nanotubes. *Angew. Chem., Int. Ed.* **2009**, *48*, 9461−9464.

(18) Gassensmith, J. J.; Kim, J. Y.; Holcroft, J. M.; Farha, O. K.; Stoddart, J. F.; Hupp, J. T.; Jeong, N. C. A Metal−Organic Framework-Based Material for Electrochemical Sensing of Carbon Dioxide. *J. Am. Chem. Soc.* **2014**, *136*, 8277−8282.

(19) Sun, C. Y.; Qin, C.; Wang, C. G.; Su, Z. M.; Wang, S.; Wang, X. L.; Yang, G. S.; Shao, K. Z.; Lan, Y. Q.; Wang, E. B. Chiral Nanoporous Metal-Organic Frameworks with High Porosity as Materials for Drug Delivery. *Adv. Mater.* **2011**, *23*, 5629−5632.

(20) Horcajada, P.; Gref, R.; Baati, T.; Allan, P. K.; Maurin, G.; Couvreur, P.; Ferey, G.; Morris, R. E.; Serre, C. Metal−Organic Frameworks in Biomedicine. *Chem. Rev.* **2012**, *112*, 1232−1268.

(21) Van de Voorde, B.; Bueken, B.; Denayer, J.; De Vos, D. Adsorptive Separation on Metal−Organic Frameworks in the Liquid Phase. *Chem. Soc. Rev.* **2014**, *43*, 5766−5788.

(22) Wang, C.; Xie, Z.; DeKrafft, K. E.; Lin, W. Doping Metal−Organic Frameworks for Water Oxidation, Carbon Dioxide Reduction, and Organic Photocatalysis. *J. Am. Chem. Soc.* **2011**, *133*, 13445−13454.

(23) Allendorf, M. D.; Schwartzberg, A.; Stavila, V.; Talin, A. A. A Roadmap to Implementing Metal−Organic Frameworks in Electronic Devices: Challenges and Critical Directions. *Chem. - Eur. J.* **2011**, *17*, 11372−11388.

(24) Alvaro, M.; Carbonell, E.; Ferrer, B.; Llabres i Xamena, F. X.; Garcia, H. Semiconductor Behavior of a Metal−Organic Framework (MOF). *Chem. - Eur. J.* **2007**, *13*, 5106−5112.

(25) Silva, C. G.; Corma, A.; García, H. Metal−Organic Frameworks as Semiconductors. *J. Mater. Chem.* **2010**, *20*, 3141−3156.

(26) Karthikeyan, M.; Bhagyaraju, B.; Mariappan, C. R.; Mobin, S. M.; Manimaran, B. Novel Semiconducting Metal−Organic Framework: Synthesis, Structural Characterisation and Electrical Conductivity Studies of Manganese Based Two Dimensional Coordination Polymer. *Inorg. Chem. Commun.* **2012**, *20*, 269−272.

(27) Sippel, P.; Denysenko, D.; Loidl, A.; Lunkenheimer, P.; Sastre, G.; Volkmer, D. Dielectric Relaxation Processes, Electronic Structure, and Band Gap Engineering of MFU-4-type Metal−Organic Frameworks: Towards a Rational Design of Semiconducting Microporous Materials. *Adv. Funct. Mater.* **2014**, *24*, 3885−3896.

(28) Gao, J.; Miao, J.; Li, P. Z.; Teng, W. T.; Yang, L.; Zhao, Y.; Liu, B.; Zhang, Q. A p-type Ti(IV)-Based Metal−Organic Framework with Visible-Light Photo-Response. *Chem. Commun.* **2014**, *50*, 3786−3788.

(29) Park, S. S.; Hontz, E. R.; Sun, L.; Hendon, C. H.; Walsh, A.; Van Voorhis, T.; Dincă, M. Cation-Dependent Intrinsic Electrical Conductivity in Isostructural Tetrathiafulvalene-Based Microporous Metal−Organic Frameworks. *J. Am. Chem. Soc.* **2015**, *137*, 1774−1777.

(30) Stavila, V.; Talin, A. A.; Allendorf, M. D. MOF-Based Electronic and Opto-Electronic Devices. *Chem. Soc. Rev.* **2014**, *43*, 5994−6010.

(31) Kobayashi, Y.; Jacobs, B.; Allendorf, M. D.; Long, J. R. Conductivity, Doping, and Redox Chemistry of a Microporous Dithiolene-Based Metal−Organic Framework. *Chem. Mater.* **2010**, *22*, 4120−4122.

(32) Ekuma, C. E.; Jarrell, M.; Moreno, J.; Bagayoko, D. First Principle Electronic, Structural, Elastic, and Optical Properties of Strontium Titanate. *AIP Adv.* **2012**, *2*, 012189.

(33) Liao, X. X.; Wang, H. Q.; Zheng, J. C. Tuning the Structural, Electronic, and Magnetic Properties of Strontium Titanate Through Atomic Design: A Comparison Between Oxygen Vacancies and Nitrogen Doping. *J. Am. Ceram. Soc.* **2013**, *96*, 538−543.

(34) Cole, M. W.; Ngo, E.; Hubbard, C.; Hirsch, S. G.; Ivill, M.; Sarney, W. L.; Zhang, J.; Alpay, S. P. Enhanced Dielectric Properties from Barium Strontium Titanate Films with Strontium Titanate Buffer Layers. *J. Appl. Phys.* **2013**, *114*, 164107.

(35) Smith, A. M.; Nie, S. Semiconductor Nanocrystals: Structure, Properties, and Band Gap Engineering. *Acc. Chem. Res.* **2010**, *43*, 190−200.

(36) Lincheneau, C.; Amelia, M.; Oszajca, M.; Boccia, A.; D'Orazi, F.; Madrigale, M.; Zanoni, R.; Mazzaro, R.; Ortolani, L.; Morandi, V.; Silvi, S.; Szaciłowski, K.; Credi, A. Synthesis and Properties of Znte And Znte/Zns Core/Shell Semiconductor Nanocrystals. *J. Mater. Chem. C* **2014**, *2*, 2877−2886.

(37) Assali, S.; Zardo, I.; Plissard, S.; Kriegner, D.; Verheijen, M. A.; Bauer, G.; Meijerink, A.; Belabbes, A.; Bechstedt, F.; Haverkort, J. E. M.; Bakkers, E. P. A. M. Direct Band Gap Wurtzite Gallium Phosphide Nanowires. *Nano Lett.* **2013**, *13*, 1559−1563.

(38) Kresse, G.; Hafner, J. *Ab Initio* Molecular Dynamics for Liquid Metals. *Phys. Rev. B: Condens. Matter Mater. Phys.* **1993**, *47*, 558−561.

(39) Kresse, G.; Hafner, J. *Ab initio* Molecular-Dynamics Simulation of the Liquid-Metal-Amorphous-Semiconductor Transition in Germanium. *Phys. Rev. B: Condens. Matter Mater. Phys.* **1994**, *49*, 14251−14269.

(40) Kresse, G.; Furthmüller, J. Efficiency of *Ab-Initio* Total Energy Calculations for Metals and Semiconductors Using a Plane-Wave Basis Set. *Comput. Mater. Sci.* **1996**, *6*, 15−50.

(41) Kresse, G.; Furthmüller, J. Efficient Iterative Schemes for *Ab Initio* Total-Energy Calculations Using a Plane-Wave Basis Set. *Phys. Rev. B: Condens. Matter Mater. Phys.* **1996**, *54*, 11169−11186.

(42) Perdew, J. P.; Burke, K.; Ernzerhof, M. Generalized Gradient Approximation Made Simple. *Phys. Rev. Lett.* **1996**, *77*, 3865−3868.

(43) Perdew, J. P.; Burke, K.; Ernzerhof, M. Generalized Gradient Approximation Made Simple. *Phys. Rev. Lett.* **1997**, *78*, 1396−1396.

(44) Blochl, P. E. Projector Augmented-Wave Method. *Phys. Rev. B: Condens. Matter Mater. Phys.* **1994**, *50*, 17953−17979.

(45) Kresse, G.; Joubert, D. From Ultrasoft Pseudopotentials to the Projector Augmented-Wave Method. *Phys. Rev. B: Condens. Matter Mater. Phys.* **1999**, *59*, 1758−1775.

(46) Monkhorst, H. J.; Pack, J. D. Special Points for Brillouin-Zone Integrations. *Phys. Rev. B* **1976**, *13*, 5188−5192.

(47) Schroder, D. K. *Semiconductor Material and Device Characterization*, 3rd Edition; John Wiley and Sons, Inc.: Hoboken, NJ, 2006.

(48) Durand, B.; Taillades, G.; Pradel, A.; Ribes, M.; Badot, J. C.; Belhadj-Tahar, N. Frequency Dependence of Conductivity in Superionic Conducting Chalcogenide Glasses. *J. Non-Cryst. Solids* **1994**, *172−174*, 1306−1314.

(49) Dutta, P.; Biswas, S.; Ghosh, M.; De, S. K.; Chatterjee, S. The DC and AC Conductivity of Polyaniline−Polyvinyl Alcohol Blends. *Synth. Met.* **2001**, *122*, 455−461.

(50) Afifi, M. A.; Bekheet, A. E.; Abd Elwahhab, E.; Atyia, H. E. AC Conductivity and Dielectric Properties of Amorphous In_2Se_3 Films. *Vacuum* **2001**, *61*, 9−17.

(51) Planchais, A.; Devautour-Vinot, S.; Salles, F.; Ragon, F.; Devic, T.; Serre, C.; Maurin, G. A Joint Experimental/Computational Exploration of the Dynamics of Confined Water/Zr-Based MOFs Systems. *J. Phys. Chem. C* **2014**, *118*, 14441−14448.

(52) Usman, M.; Lee, C. H.; Hung, D. S.; Lee, S. F.; Wang, C. C.; Luo, T. T.; Zhao, L.; Wu, M. K.; Lu, K. L. Intrinsic Low Dielectric Behaviour of a Highly Thermally Stable Sr-Based Metal−Organic Framework for Interlayer Dielectric Materials. *J. Mater. Chem. C* **2014**, *2*, 3762−3768.

(53) Jonscher, A. K. The 'Universal' Dielectric Response. *Nature* **1977**, *267*, 673−679.

(54) Zhou, B.; Kobayashi, A.; Cui, H.-B.; Long, L.-S.; Fujimori, H.; Kobayashi, H. Anomalous Dielectric Behavior and Thermal Motion of Water Molecules Confined in Channels of Porous Coordination Polymer Crystals. *J. Am. Chem. Soc.* **2011**, *133*, 5736−5739.

(55) Zhao, H. X.; Liu, J. X.; Long, L. S.; Bokov, A. A.; Ye, Z. G.; Huang, R. B.; Zheng, L. S. High Dielectric Constant and Relaxation Mechanism of Water with Hydrated Copper(II) Ions in a Cucurbit[8]uril-Based Supramolecular Architecture. *J. Phys. Chem. C* **2012**, *116*, 14199−14204.

(56) Liao, W. Q.; Zhang, Y.; Hu, C. L.; Mao, J. G.; Ye, H. Y.; Li, P. F.; Huan, S. D.; Xiong, R. G. A Lead-Halide Perovskite Molecular Ferroelectric Semiconductor. *Nat. Commun.* **2015**, *6*, 8338−8344.

(57) Tauc, J.; Grigorovici, R.; Vancu, A. Optical Properties and Electronic Structure of Amorphous Germanium. *Phys. Status Solidi B* **1966**, *15*, 627−637.

(58) Wang, X. W.; Chen, J. Z.; Liu, J. H. Photoluminescent Zn(II) Metal−Organic Frameworks Built from Tetrazole Ligand: 2D Four-Connected Regular Honeycomb (4363)-net. *Cryst. Growth Des.* **2007**, *7*, 1227−1229.

(59) Butler, K. T.; Hendon, C. H.; Walsh, A. Electronic Chemical Potentials of Porous Metal−Organic Frameworks. *J. Am. Chem. Soc.* **2014**, *136*, 2703−2706.

(60) Zagorodniy, K.; Seifert, G.; Hermann, H. Metal−Organic Frameworks as Promising Candidates for Future Ultralow-κ Dielectrics. *Appl. Phys. Lett.* **2010**, *97*, 251905.